A&A, 687, A220 (2024)
https://doi.org/10.1051/0004-6361/202449918

Astronomy & Astrophysics

Rotational spectroscopy of CH_3OD with a reanalysis of CH_3OD toward IRAS 16293−2422⋆

V. V. Ilyushin[1], H. S. P. Müller[2], M. N. Drozdovskaya[3], J. K. Jørgensen[4], S. Bauerecker[5], C. Maul[5], R. Porohovoi[1], E. A. Alekseev[1,6], O. Dorovskaya[1], O. Zakharenko[2], F. Lewen[2], S. Schlemmer[2], L.-H. Xu[7], and R. M. Lees[7]

[1] Institute of Radio Astronomy of NASU, Mystetstv 4, 61002 Kharkiv, Ukraine
e-mail: ilyushin@rian.kharkov.ua
[2] Astrophysik/I. Physikalisches Institut, Universität zu Köln, Zülpicher Str. 77, 50937 Köln, Germany
e-mail: hspm@ph1.uni-koeln.de
[3] Physikalisch-Meteorologisches Observatorium Davos und Weltstrahlungszentrum (PMOD/WRC), Dorfstrasse 33, 7260, Davos Dorf, Switzerland
[4] Niels Bohr Institute, University of Copenhagen, Øster Voldgade 5−7, 1350 Copenhagen K, Denmark
[5] Institut für Physikalische und Theoretische Chemie, Technische Universität Braunschweig, Gaußstr. 17, 38106 Braunschweig, Germany
[6] Univ. Lille, CNRS, UMR 8523 – PhLAM – Physique des Lasers Atomes et Molécules, 59000 Lille, France
[7] Department of Physics, University of New Brunswick, Saint John, NB E2L 4L5, Canada

Received 9 March 2024 / Accepted 27 May 2024

ABSTRACT

We have started a measurement campaign of numerous methanol isotopologs in low-lying torsional states in order to provide extensive line lists for radio astronomical observations from an adequate spectroscopic model and to investigate how the intricate vibration-torsion-rotation interactions manifest themselves in the spectra of different isotopic species. After CD_3OH and CD_3OD, we turn our focus to CH_3OD, which is an important species for studying deuteration in prestellar cores and envelopes that enshroud protostars. Notably, deuteration is frequently viewed as a diagnostic tool for star formation. The measurements used in this study were obtained in two spectroscopic laboratories and cover large fractions of the 34 GHz−1.35 THz range. As done in previous studies, we employed a torsion-rotation Hamiltonian model for our analysis that is based on the rho-axis method. The resulting model describes the ground and first excited torsional states of CH_3OD well up to quantum numbers $J \leqslant 51$ and $K_a \leqslant 18$. We derived a line list for radio astronomical observations from this model that is accurate up to at least 1.35 THz and should be sufficient for all types of radio astronomical searches for this methanol isotopolog in these two lowest torsional states. This line list was applied to a reinvestigation of CH_3OD in data from the Protostellar Interferometric Line Survey of IRAS 16293−2422 obtained with the Atacama Large Millimeter/submillimeter Array. The new accurately determined value for the column density of CH_3OD implies that the deuteration in methanol differs in its two functional groups by a factor of ∼7.5.

Key words. astrochemistry – molecular data – methods: laboratory: molecular – techniques: spectroscopic – ISM: molecules – ISM: individual objects: IRAS 16293–2422

1. Introduction

The singly deuterated methanol isotopolog CH_3OD was detected unambiguously by Mauersberger et al. (1988), about twenty years after the detection of CH_3OH (Ball et al. 1970). Since then, CH_3OD has become an important diagnostic tool for the degree of deuteration in star-forming regions (Ratajczak et al. 2011; Neill et al. 2013; Bøgelund et al. 2018; Jørgensen et al. 2018; Taquet et al. 2019; Wilkins & Blake 2022; Okoda et al. 2022). The degree of deuteration in turn has been considered an indicator of the conditions of star formation (Crapsi et al. 2005; Ceccarelli et al. 2007; Fontani et al. 2011; Chantzos et al. 2018) and has even been used to estimate the age of a star-forming region (Brünken et al. 2014; Harju et al. 2017).

High degrees of methanol deuteration have been found in several hot corinos (which are the warm and dense inner parts of low-mass star-forming regions), including IRAS 16293−2422 B (Jørgensen et al. 2018; Taquet et al. 2019). Furthermore, enhanced methanol deuteration has been demonstrated in the cold envelope of the low-mass Class 0 source L483 (Agúndez et al. 2019) and several starless prestellar cores, including L1544 (Chacón-Tanarro et al. 2019; Ambrose et al. 2021; Lin et al. 2023). However, the deuterium enrichment in methanol is less pronounced in high-mass star-forming regions (Bøgelund et al. 2018; van Gelder et al. 2022) and even less so if the high-mass star-forming regions reside in the Galactic center, such as Sagittarius B2(N2) (Belloche et al. 2016).

The rotational spectra of CH_3OD and other methanol isotopologs were first observed in the laboratory in the 1950s, and the initial goal was to determine their molecular structure (Venkateswarlu et al. 1955). Similar measurements were carried out by Nishikawa (1956), who also evaluated the height of the potential barrier to internal rotation based on CH_3OD data at 371 ± 5 cm^{-1}. Lees & Baker (1968) published the first extensive study of its rotational spectrum in the millimeter wave region by investigating the torsion-rotation interaction

⋆ Electronic supplementary material for this work can be found at https://doi.org/10.5281/zenodo.11460242

in the methanol isotopologs CH_3OH, CD_3OH, and CH_3OD up to 200 GHz. The compilation of Lovas (1986) contained some unpublished CH_3OD data near 90 GHz taken by Lovas and Suenram in 1978. Additional measurements in the 14–92 GHz range were subsequently published by Kaushik et al. (1980), who also determined the dipole moment components through Stark effect measurements. The dipole moment components were redetermined shortly thereafter (Takagi & Kaushik 1982). Anderson et al. (1988) expanded assignments of CH_3OD in the ground torsional state $v_t = 0$ well into the submillimeter region. Some time later, Anderson et al. (1993) made further assignments, including several in $v_t = 1$. Two subsequent studies by Walsh et al. (2000) and Duan et al. (2003) extended assignments to $v_t = 2$. Both studies benefited from far-infrared laboratory measurements (e.g., Mukhopadhyay et al. 1997, 1998; Mukhopadhyay 1999; Mukhopadhyay & Duan 2000). In addition, several high-resolution infrared studies have been published. Important for our investigations are the works on the CO stretching band at 1042.7 cm^{-1} (Lundsgaard et al. 1994) and on the COD bending mode at 863.2 cm^{-1} with a less detailed account of its hot band (Lees et al. 2013). These two publications indicate interactions between the CO stretching state, the combination state of the COD bending with one quantum of the torsion, and $v_t = 4$. In the course of our investigation, a report appeared on millimeter to far-infrared spectra of CH_3OD with a redetermination of its dipole moment components (Mukhopadhyay 2021).

We have embarked on a program to extensively study various methanol isotopologs in low-lying torsional states in order to develop line lists with reliable positions and line strengths for astronomical observations and to investigate the intricate vibration-torsion-rotation interactions in their spectra. After our first reports on CD_3OH (Ilyushin et al. 2022) and CD_3OD (Ilyushin et al. 2023), we have turned our attention to CH_3OD. We performed new measurements in the millimeter and submillimeter ranges to expand the frequency range with microwave accuracy up to 1.35 THz. The new data were combined in particular with previously published far-infrared measurements to form the final dataset involving rotational quantum numbers up to $J = 51$ and $K = 18$. A fit within the experimental errors was obtained for the ground and first excited torsional states of CH_3OD by employing the so-called rho-axis-method.

We generated a line list that is based on our present results, which we applied to a reanalysis of CH_3OD in ALMA data of the Protostellar Interferometric Line Survey (PILS, Jørgensen et al. 2016) of the deeply embedded protostellar system IRAS 16293−2422. The new spectroscopic information leads to a lower column density in this source in comparison to the earlier determinations. This has major implications for our understanding of deuteration in the two functional groups of methanol.

The rest of the manuscript is organized as follows. Section 2 provides details on our laboratory measurements. The theoretical model, spectroscopic analysis, and fitting results are presented in Sects. 3 and 4. Section 5 describes our astronomical observations and the results of our present CH_3OD analysis, while Sect. 6 provides the conclusions of our current investigation.

2. Experimental details

2.1. Rotational spectra at the Universität zu Köln

The spectral recordings at the Universität zu Köln were carried out at room temperature using two different spectrometers. Pyrex glass cells of different lengths and with an inner diameter of 100 mm were employed. The cells were equipped with Teflon windows below ~500 GHz; high-density polyethylene was used at higher frequencies. A commercial sample of CH_3OD (Sigma-Aldrich) was employed at initial pressures of 1.5 to 2.0 Pa. Minute leaks in the cells required a refill after several hours because of the slowly increasing pressure. These leaks caused some D-to-H exchange despite conditioning of the cells with higher pressures of CH_3OD prior to the measurements. The resulting lines of CH_3OH did not pose any problem in the analyses because they can be easily identified from the work of Xu et al. (2008).

Both spectrometer systems used Virginia Diode, Inc. (VDI), frequency multipliers driven by Rohde & Schwarz SMF 100A microwave synthesizers as sources. Schottky diode detectors were utilized below ~500 GHz, whereas liquid He-cooled InSb bolometers (QMC Instruments Ltd) were applied between ~500 and 1346 GHz. Frequency modulation was used throughout, and the demodulation at $2f$ caused an isolated line to appear close to a second derivative of a Gaussian.

A double pass cell of 5 m in length was used to cover the 155−510 GHz range. Further information on this spectrometer is available elsewhere (Martin-Drumel et al. 2015). We achieved frequency accuracies of 5 kHz for the best lines with this spectrometer in a study of 2-cyanobutane (Müller et al. 2017), which exhibits a much richer rotational spectrum. We employed a setup with a 5-m single pass cell to cover 494 to 750 GHz, 760 to 1093 GHz, and several sections of the 1117 to 1346 GHz region. Additional information on this spectrometer system is available in Xu et al. (2012). We were able to achieve uncertainties of 10 kHz and even better for very symmetric lines with very good signal-to-noise (S/N) ratios, as demonstrated in recent studies on excited vibrational lines of CH_3CN (Müller et al. 2021) and on isotopic oxirane (Müller et al. 2022, 2023). Uncertainties of 10, 20, 30, 50, 100, and 200 kHz were assigned in the present study, depending on the symmetry of the line shape, the S/N, and the frequency range. The smallest uncertainties above 1.1 THz were 50 kHz.

2.2. Rotational spectra at IRA NASU

The measurements of the CH_3OD spectrum at the Institute of Radio Astronomy (IRA) of the National Academy of Sciences of Ukraine (NASU) were performed in the frequency ranges 34.4−183 GHz and 234−420 GHz using an automated synthesizer-based millimeter wave spectrometer (Alekseev et al. 2023). This instrument belongs to a class of absorption spectrometers and uses a set of backward wave oscillators (BWO) to cover the frequency range from 34.4 to 183 GHz, allowing further extension to the 234−420 GHz range employing a solid state tripler from VDI. The frequency of the BWO probing signal was stabilized by a two-step frequency multiplication of a reference synthesizer in two phase-lock-loop stages. A commercial sample of CH_3OD was used, and all measurements were carried out at room temperature, with sample pressures providing line widths close to the Doppler-limited resolution (about 2 Pa). The recorded spectrum contains numerous CH_3OH lines because of the relatively fast D-to-H exchange, as was observed at the Universität zu Köln. Estimated uncertainties for measured line frequencies were 10, 30, and 100 kHz, depending on the observed S/N.

3. Spectroscopic properties of CH_3OD and our theoretical approach

The theoretical approach that we employed in the present study is the so-called rho-axis-method (RAM), which has proven to

be the most effective approach so far in treating torsional large-amplitude motions in methanol-like molecules. The method is based on the work of Kirtman (1962), Lees & Baker (1968), and Herbst et al. (1984) and takes its name from the choice of its axis system (Hougen et al. 1994). In RAM, the z axis is coincident with the ρ vector, which expresses the coupling between the angular momentum of the internal rotation p_α and that of the global rotation J. We employed the RAM36 code (Ilyushin et al. 2010, 2013), which was successfully used in the past for a number of near-prolate tops with rather high ρ and J values (see, e.g., Smirnov et al. 2014; Motiyenko et al. 2020; Zakharenko et al. 2019, and Bermudez et al. 2022) and in particular for the CD_3OH and CD_3OD isotopologs of methanol (Ilyushin et al. 2022, 2023). The RAM36 code uses the two-step diagonalization procedure of Herbst et al. (1984), and in the current study, we kept 41 torsional basis functions at the first diagonalization step and 11 torsional basis functions at the second diagonalization step.

The OD-deuterated methanol, CH_3OD, is a nearly prolate top ($\kappa \approx -0.966$) with a rather high coupling between internal and overall rotations in the molecule ($\rho \approx 0.699$). Its torsional potential barrier V_3 is about 366 cm^{-1}. The torsional problem in CH_3OD corresponds to an intermediate barrier case (Lin & Swalen 1959) with the reduced barrier $s = 4V_3/9F$ ~9.3, where F is the rotation constant of the internal rotor. In comparison to the parent isotopolog, CH_3OD has somewhat smaller rotational parameters: $A \approx 3.68$ cm^{-1}, $B \approx 0.783$ cm^{-1}, and $C \approx 0.733$ cm^{-1} in CH_3OD versus $A \approx 4.25$ cm^{-1}, $B \approx 0.823$ cm^{-1}, and $C \approx 0.792$ cm^{-1} in CH_3OH (Xu et al. 2008). The angle between the RAM a-axis and the principal-axis-method (PAM) a-axis is 0.55°, which is significantly larger than the corresponding angle of 0.07° in the parent methanol isotopolog. This larger angle in combination with its higher asymmetry ($\kappa \approx -0.966$ in CH_3OD versus $\kappa \approx -0.982$ in CH_3OH) leads to a situation where the labeling scheme after the second diagonalization step based on searching for a dominant eigenvector component starts to fail for some eigenvectors at $J \approx 24$. That is why we employed a so-called combined labeling scheme, where we used a dominant eigenvector component (≥0.8), if it exists, and we searched for similarities in the basis-set composition between the current eigenvector and the torsion–rotation eigenvectors belonging to the previous J value and assigned the level according to the highest similarity found if a dominant eigenvector component is absent. This approach has already been applied successfully in the case of the CD_3OD study (Ilyushin et al. 2023), where a more detailed description may be found. Further details of this labeling approach for torsion–rotation energy levels in low-barrier molecules based on similarities in basis-set composition of torsion–rotation eigenvectors of adjacent J can be found in Ilyushin (2004).

The energy levels in our fits and predictions are labeled by the free rotor quantum number m, the overall rotational angular momentum quantum number J, and a signed value of K_a, which is the axial a-component of the overall rotational angular momentum J. In the case of the A symmetry species, the +/− sign corresponds to the so-called parity designation, which is related to the A1/A2 symmetry species in the group G_6 (Hougen et al. 1994). The signed value of K_a for the E symmetry species reflects the fact that the Coriolis-type interaction between the internal rotation and the global rotation causes levels with $|K_a| > 0$ to split into a $K_a > 0$ level and a $K_a < 0$ level. We also provide K_c values for convenience, but they are simply recalculated from the J and K_a values: $K_c = J - |K_a|$ for $K_a \geq 0$ and $K_c = J - |K_a| + 1$ for $K_a < 0$. The m values 0, −3, 3/1, −2, and 4 correspond to A/E transitions of the v_t = 0, 1, and 2 torsional states, respectively.

4. Spectroscopic results

We started our analysis from the microwave part of the dataset available in Tables 2 and 3 of Duan et al. (2003), which consists of 994 $v_t \leq 2$ microwave transitions ranging up to $J_{max} = 21$ and $K_{max} = 9$ augmented by the far-infrared measurements available in Table 2 of Mukhopadhyay & Duan (2000). As a first step, we analyzed this combined dataset using the RAM36 program (Ilyushin et al. 2010, 2013) and used the resulting fit as the starting point for our assignments. New data were assigned starting with the Kharkiv measurements, which were done in parallel for the three lowest torsional states of CH_3OD v_t = 0, 1, and 2. Submillimeter wave and terahertz measurements from Köln were assigned subsequently based on our new results. The assignment process was performed in a usual bootstrap manner, with numerous cycles of refinement of the parameter set while gradually adding the new data. Whenever it was possible, we replaced the old measurements from Duan et al. (2003) and references therein with the more accurate new ones. In the best case, this gave us an improvement in measurement uncertainty from 100 kHz to 10 kHz, whereas in the worst case, a reduction of uncertainty from 50 kHz to 30 kHz was achieved. At the same time, as we already did in the cases of the CD_3OH (Ilyushin et al. 2022) and CD_3OD (Ilyushin et al. 2023) studies, we decided to keep the two measured values for the same transition in the fits from the Kharkiv and Köln spectral recordings in that part of the frequency range where the measurements from the two laboratories overlap (154−183 GHz and 234−420 GHz). A rather good agreement within the experimental uncertainties was observed for this limited set of duplicate new measurements. Finally, at an advanced stage of our analysis, the far-infrared data from Mukhopadhyay (2021) were added to the fit.

In the process of searching for the optimal set, it became evident that the v_t = 2 torsional state poses some problems with fitting. The strong influence of intervibrational interactions arising from low-lying small-amplitude vibrations in CH_3OD (see, for example, Lundsgaard et al. 1994; Lees et al. 2013), which then propagate down through numerous intertorsional interactions, is a possible explanation for these problems. We encountered similar problems with CD_3OH (Ilyushin et al. 2022) and CD_3OD (Ilyushin et al. 2023). In the future, we plan to account explicitly for the above-mentioned intervibrational interactions, and with this aim in mind, new measurements of the CH_3OD IR spectrum between 500 and 1200 cm^{-1} were carried out at the Technische Universität Braunschweig. These measurements were not used in the present investigation. Therefore, the details of these new measurements will be presented in due course when the new data will be included in our analysis of intervibrational interactions. In the meantime, the difficulties in fitting the v_t = 2 data within experimental uncertainties prompted us to limit our analysis mainly to the ground and first excited torsional states, thus providing reliable rest frequencies for radio astronomical observations of CH_3OD. At the final stage of the model refinement, our fit included, besides the ground and first excited torsional states of CH_3OD, the lowest three K series for the A and E species in v_t = 2 in order to obtain a better constraint of the torsional parameters in the Hamiltonian model. These v_t = 2 K levels should be the least affected by the intervibrational interactions arising from low-lying small-amplitude vibrations. In the case of CH_3OD, this corresponds to

Table 1. Overview of the dataset and the fit quality.

By measurement uncertainty			By torsional state		
Unc. [a]	# [b]	rms [c]	v_t [d]	# [b]	wrms [e]
0.010 MHz	5198	0.0085 MHz	$v_t = 0 \leftarrow 0$	6847	0.82
0.020 MHz	932	0.0169 MHz	$v_t = 1 \leftarrow 1$	5694	0.88
0.030 MHz	1095	0.0246 MHz	$v_t = 2 \leftarrow 2$	363	0.89
0.050 MHz	1224	0.0389 MHz	$v_t = 1 \leftarrow 0$	3330	0.94
0.100 MHz	1086	0.0765 MHz	$v_t = 2 \leftarrow 1$	346	0.87
0.200 MHz	628	0.1382 MHz	$v_t = 1 \leftarrow 2$	3	0.62
2×10^{-4} cm^{-1}	4758	1.8×10^{-4} cm^{-1}			

Notes. [a]Estimated measurement uncertainties for each data group. [b]Number of lines (left part) or transitions (right part) of each category in the least-squares fit. We note that due to blending, 14 921 measured line frequencies correspond to 16 583 transitions in the fit, which in turn due to the presence of duplicate measurements represent 15 049 unique transitions in the fit. [c]Root mean square deviation of corresponding data group. [d]Upper- and lower-state torsional quantum number v_t. [e]Weighted root mean square deviation of the corresponding data group.

$K = -1, -2, 3$ for the E species in $v_t = 2$ and to $K = -1, 0, 1$ for the A species.

Our final CH_3OD dataset contains 4758 far-infrared and 10 163 microwave line frequencies. Due to blending, these 14 921 measured frequencies correspond to 16 583 transitions with $J_{max} = 51$ and $K_a \leqslant 18$. Taking into account duplicate measurements mentioned above, our final dataset represents 15 049 unique transitions in the fit. A Hamiltonian model consisting of 134 parameters provided a fit with a weighted root mean square (wrms) deviation of 0.85, which was selected as our "best fit" for this paper. The 134 molecular parameters from our final fit are given in Table A.1. The numbers of the terms in the model distributed between the orders $n_{op} = 2$, 4, 6, 8, 10, 12 are 7, 22, 46, 39, 16, 4, respectively, which is consistent with the limits of determinable parameters of 7, 22, 50, 95, 161, and 252 for these orders, as calculated from the differences between the total number of symmetry-allowed Hamiltonian terms of order n_{op} and the number of symmetry-allowed contact transformation terms of order $n_{op} - 1$ when applying the ordering scheme of Nakagawa et al. (1987). The final set of the parameters converged perfectly in all three senses: (i) the relative change in the wrms deviation of the fit at the last iteration was about $\sim 5 \times 10^{-7}$; (ii) the corrections to the parameter values generated at the last iteration were less than $\sim 10^{-3}$ of the calculated parameter confidence intervals; and (iii) the changes generated at the last iteration in the calculated frequencies were less than 1 kHz, even for the far-infrared data.

A summary of the quality of this fit is given in Table 1. In the left part of Table 1, the data are grouped by measurement uncertainty, and all data groups are fit within experimental uncertainties. We observed the same good agreement in the right part of Table 1, where the data are grouped by torsional state. The overall wrms deviation of the fit is 0.85. A further illustration of the rather good agreement between the observed and the calculated line positions and intensities from our final Hamiltonian model in the spectrum of CH_3OD can be seen in Figs. 1 and 2.

We calculated a CH_3OD line list in the ground and first excited torsional states from the parameters of our final Hamiltonian model for radio astronomical observations. The dipole moment function of Mekhtiev et al. (1999) was employed in our calculations where the values for the permanent dipole moment components of CH_3OH were replaced by appropriate ones for CH_3OD; $\mu_a = 0.8343$ D and $\mu_b = 1.4392$ D were taken from Mukhopadhyay (2021). The permanent dipole moment components were rotated from the principal axis system to the rho axis

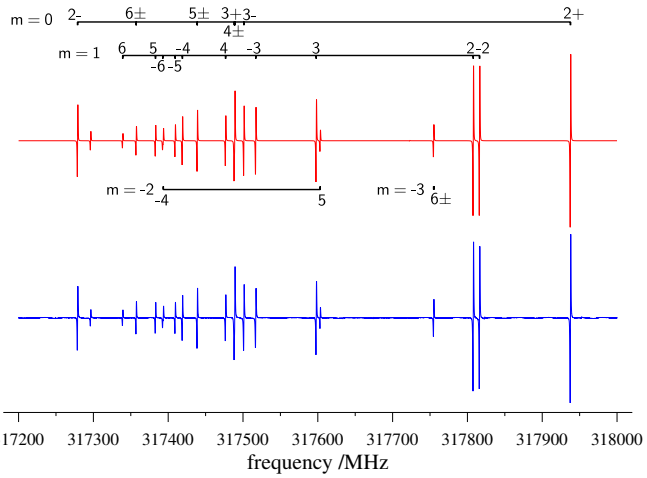

Fig. 1. Portion of the CH_3OD microwave spectrum dominated by the $J = 7 \leftarrow 6$ R-branch of transitions in the 317.2–318.0 GHz range. The observed spectrum is shown in the lower panel, and the calculated one is in the upper panel. The spectrum was recorded in the first derivative detection mode of the Kharkiv spectrometer. The K quantum numbers for the $m = 0, 1$ ($v_t = 0$) transitions are given above, and for the $m = -2, -3$ ($v_t = 1$) transitions, they are given below the simulated spectrum in the upper panel. We observed that the experimental frequencies and the intensity pattern are rather well reproduced by our model for the spectral features dominating this frequency range.

system of our Hamiltonian model. As in the cases of CD_3OH (Ilyushin et al. 2022) and CD_3OD (Ilyushin et al. 2023), the list of CH_3OD transitions includes information on transition quantum numbers, transition frequencies, calculated uncertainties, lower-state energies, and transition strengths. As already mentioned, we labeled torsion-rotation levels by the free rotor quantum number m, the overall rotational angular momentum quantum number J, a signed value of K_a, and K_c. To avoid unreliable extrapolations far beyond the quantum number coverage of the available experimental dataset, we limited our predictions by $v_t \leq 1$, $J \leq 55$ and $|K_a| \leq 21$. The calculations were done up to 2.0 THz. Additionally, we limited our calculations to transitions for which calculated uncertainties are less than 0.1 MHz. The lower-state energies are given referenced to the $J = 0$ A-type $v_t = 0$ level. In addition, we provide the torsion-rotation part of the partition function $Q_{rt}(T)$ of CH_3OD calculated from first principles, that is, via direct summation over the torsion-rotational

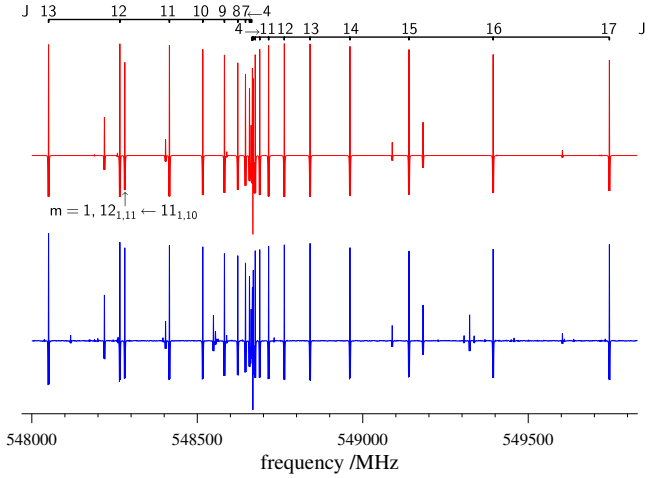

Fig. 2. Portion of the CH_3OD microwave spectrum dominated by the $m = 0$ $K = 4\pm \leftarrow 3\mp$ Q-branch transitions in the 548.0–549.8 GHz range. The observed spectrum is shown in the lower panel, and the calculated one is in the upper panel. The spectrum was recorded in the second derivative detection mode of the Köln spectrometer. The J quantum numbers of the Q-branch transitions given at the top decrease with frequency for the $K = 4+ \leftarrow 3-$ transitions and increase with frequency for the $K = 4- \leftarrow 3+$ transitions. The arrows in progressions of J quantum numbers shown in the top panel indicate the successive J values (from four to seven for $K = 4+ \leftarrow 3-$ and from four to 11 for $K = 4- \leftarrow 3+$) that we were not able to show separately within the selected scale of the figure. Also, we have marked the $m = 1$, $12_{1,11} \leftarrow 11_{1,10}$ R-type transition, which has a comparable intensity with dominating Q-branch transitions in this range. We observed that the experimental frequencies and the intensity pattern are rather well reproduced by our model for the spectral features dominating this frequency range.

states. The maximum J value is 65 for this calculation, and $n_{v_t} = 11$ torsional states were taken into account. The calculations, as well as the experimental line list from the present work, can be found in the online supplementary material of this article and will also be available in the Cologne Database for Molecular Spectroscopy (CDMS, Müller et al. 2001, 2005; Endres et al. 2016).

5. CH_3OD in IRAS 16293-2422

The new spectroscopic calculations were used to reanalyze the emission lines of CH_3OD in data from the Protostellar Interferometric Line Survey (PILS[1]; project-id: 2013.1.00278.S, PI: Jes K. Jørgensen). PILS represents an unbiased spectral line survey of the Class 0 protostellar system IRAS 16293-2422 using ALMA and covering the frequency range from 329 to 363 GHz. The observations target the region of IRAS 16293-2422, including its two primary components "A" and "B" that show abundant lines of complex organic molecules at an angular resolution of ~0.5″ and a spectral resolution of ~0.2 km s^{-1}. Toward a position slightly offset from the "B" component of the system (RA, Dec (J2000) of $16^h32^m22.58^s$, $-24°28'32.80''$), the lines are intrinsically narrow, making it an ideal hunting ground for new species. Several complex organic molecules and their isotopologs have already been identified there, including deuterated isotopologs of CH_3OH, namely CH_2DOH and CH_3OD (Jørgensen et al. 2018), CHD_2OH (Drozdovskaya et al. 2022), and CD_3OH (Ilyushin et al. 2022). A tentative detection of several CD_3OD lines has also been reported at this position (Ilyushin et al. 2023). The full details on the PILS dataset and its reduction are available in Jørgensen et al. (2016).

The reanalysis of CH_3OD was conducted by fitting synthetic spectra to the observations with calculations that assume that the excitation of the molecule is characterized by local thermodynamical equilibrium (LTE), which is reasonable at the densities on the spatial scales probed by PILS (namely, H_2 number density $>3 \times 10^{10}$ cm^{-3}, which was demonstrated to result in deviations between the excitation and kinetic temperatures of less than 15%; Sect. 5.1 of Jørgensen et al. 2016). For all CH_3OD lines, the velocity offset relative to the local standard of rest matches the canonical 2.7 km s^{-1} at this position, and its line widths are well fit by the typical 1 km s^{-1} full width half maximum (FWHM). Beam size and source size were both fixed to 0.5″ and were both assumed to have Gaussian distributions (i.e., beam-filling factor of 0.5). The fitting methodology is based on the MCMC Python package EMCEE (Foreman-Mackey et al. 2013)[2], and its application is described in detail in Sect. 2.3 of Drozdovskaya et al. (2022). There are in total 485 lines of CH_3OD (243 in $v_t = 0$ and 242 in $v_t = 1$) covered in the observed PILS frequency range, of which 480 (241 in $v_t = 0$ and 239 in $v_t = 1$) have unique rest frequencies. All covered (detected and non-detected) lines of CH_3OD were investigated for potential blending with already identified molecules in this source. All lines that have any level of blending were removed from further synthetic spectrum fitting. Optically thick lines of CH_3OD were also removed from further synthetic spectrum fitting. These are assumed to be lines that have $\tau > 0.1$ either at $T_{ex} = 50$ or 300 K at $N = 4.5 \times 10^{16}$ cm^{-2} (the best-fit column density of CH_3OD derived in Jørgensen et al. 2018, corrected for the factor of four error discussed below). After the removal of the blended and optically thick lines, 97 unique line frequencies remained, and they were then used for synthetic spectral fitting (this includes detected and non-detected lines). Out of the 97 lines, 28 were predicted to have a peak intensity greater than 14 mJy beam^{-1} (and an integrated intensity greater than 3σ for $\sigma = 4.5$ mJy beam^{-1} km s^{-1} and a line width of 1 km s^{-1}) for the subsequently derived best-fitting T_{ex} and N (Table 2). In this way, non-blended, non-detected lines were also used to constrain the synthetic spectral fitting. The number of walkers and the parameter space setup used here match what was used for the analysis of CHD_2OH in Drozdovskaya et al. (2022). Only for the case of fitting CH_3OD in the $v_t = 0$ and $v_t = 1$ states together, the number of steps had to be increased from 1 000 to 1 500 to ensure proper convergence. For the second MCMC run of the computation, the mean acceptance fraction of the 300 walkers is 70 – 71% (independent of whether the $v_t = 0$ and $v_t = 1$ states were fitted together or separately), and the quality of the convergence is illustrated in the corner plot shown in Fig. B.1 for IRAS 16293-2422 B.

Fitting the $v_t = 0$ and 1 states simultaneously yields a best-fitting $T_{ex} = 190 \pm 19$ K and $N = (3.25 \pm 0.65) \times 10^{16}$ cm^{-2} (Table 2, Fig. 3). If the two v_t states are fitted separately, then it becomes apparent that the fit is driven to $T_{ex} < 200$ K based on the $v_t = 1$ lines. However, the $v_t = 0$ lines are best fit by $T_{ex} \approx 200$ K, which, considering the error bars, cannot be firmly ascertained as stemming from a component of a different temperature. The differences in N for the range of best-fitting T_{ex} depending on whether the v_t states are fit together or separately are less than a factor of 1.6. Hence, there is no reason to fit the $v_t = 0$ and 1 states of CH_3OD separately in the PILS data.

[1] http://youngstars.nbi.dk/PILS/

[2] https://emcee.readthedocs.io/en/stable/

Table 2. Best-fitting column densities, excitation temperatures, and D/H ratios of CH_3OD toward IRAS 16293-2422 B.

Best-fitting parameters	IRAS 16293-2422 B
Fitting v_t = 0 and 1 together	
T_{ex} (K)	190 ± 19
$N(CH_3OD_{v_t=0,1})$ (cm^{-2})	$(3.25 \pm 0.65) \times 10^{16}$
D/H of CH_3OH	$(3.2 \pm 0.9) \times 10^{-3}$
# lines	97
E_{up} range (K)	124 – 2969
Fitting solely v_t = 0	
T_{ex} (K)	205 ± 21
$N(CH_3OD_{v_t=0})$ (cm^{-2})	$(2.52 \pm 0.50) \times 10^{16}$
D/H of CH_3OH	$(2.5 \pm 0.7) \times 10^{-3}$
# lines	46
E_{up} range (K)	124 – 2969
Fitting solely v_t = 1	
T_{ex} (K)	163 ± 16
$N(CH_3OD_{v_t=1})$ (cm^{-2})	$(4.01 \pm 0.80) \times 10^{16}$
D/H of CH_3OH	$(4.0 \pm 1.0) \times 10^{-3}$
# lines	51
E_{up} range (K)	332 – 2287

Notes. Top part contains the best-fitting column density and excitation temperature of CH_3OD obtained during simultaneous fitting of these two parameters for both v_t = 0 and 1 states together and the associated D/H ratio. We note that the statistical correction on the D/H ratio for the case of deuteration in the hydroxy group is one (Appendix C of Drozdovskaya et al. 2022; see also Manigand et al. 2019). The fitting has also been executed for the two v_t states separately, for which the corresponding derived column densities and D/H ratios are the middle and lower parts, respectively. The second column contains the values for the one-beam offset position in the SW direction from IRAS 16293-2422 B (0.5″ or 70 au away from the dust peak of B). For the calculations of D/H ratios, the adopted methanol column densities is $(1.0 \pm 0.2) \times 10^{19}$ cm^{-2} (Jørgensen et al. 2018). The stated errors on N and T_{ex} are assumed 20% and 10% errors, respectively. The errors derived with the MCMC routine in this work are much smaller (we refer to Drozdovskaya et al. (2022) for a discussion about that). For each of the three fitting scenarios, the number of lines with unique frequencies used for the fitting and the E_{up} range spanned by these lines are also provided.

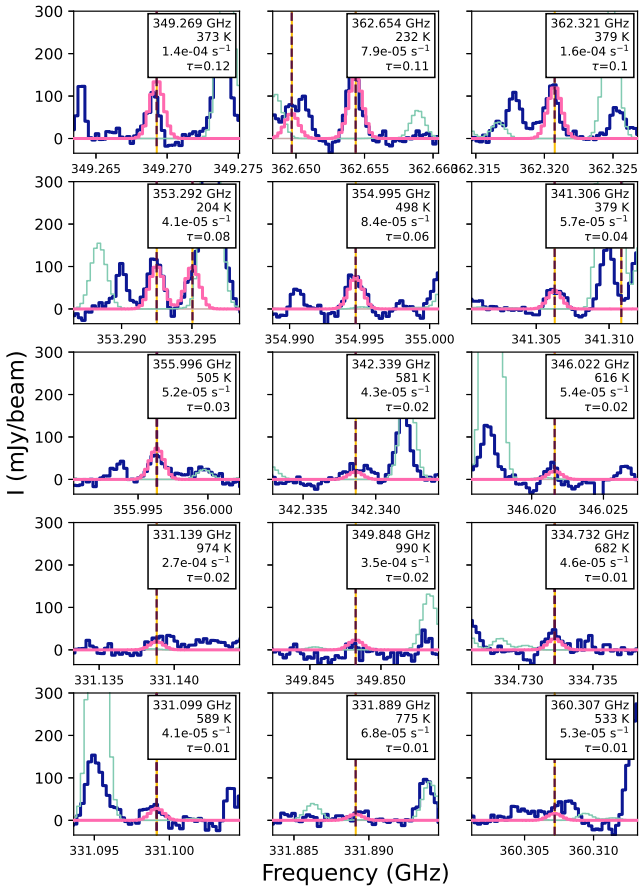

Fig. 3. Selection of 15 detected lines of CH_3OD ordered by their line opacity (τ) from top left to bottom right. The observed spectrum is in dark blue, the reference spectrum (corresponding to all other species identified thus far in PILS) is in turquoise, and the best-fitting synthetic spectrum of CH_3OD is in pink. The rest frequency, E_{up} (K), A_{ij} (s^{-1}), and τ (for the best-fitting parameters) are shown in the right corner of each panel. The rest frequency is indicated with a vertical dashed line, and the filled yellow region corresponds to the uncertainty on that line frequency. The lines at 355.996, 334.732, and 331.099 GHz are in fact unresolved asymmetry doublets. Only the panels corresponding to 341.306, 355.996, 342.339, 346.022, 334.732, 331.099, 331.889, and 360.307 GHz illustrate lines that have been included in constraining the best-fit synthetic spectrum, as the others become (partially) optically thick ($\tau > 0.1$) at T_{ex} = 50 K, 300 K, or both.

Using the new spectroscopic data significantly reduces the best-fitting T_{ex} and N for CH_3OD in comparison to the earlier estimates in Jørgensen et al. (2018) of $N = 1.8 \times 10^{17}$ cm^{-2} and T_{ex} = 300 K, which corresponds to a reduction by a factor of ∼5.5 in N and ∼1.6 in T_{ex}. Part of this difference in the column density is due to an incorrect coupling between the partition function for CH_3OD and the line intensities for the spectroscopic data utilized in Jørgensen et al. (2018). For the partition function, that paper utilized a scaled version of the partition function for $CH_3^{18}OH$ but did not take into account the factor for g_I. This factor was equal to one for the CH_3OD intensities from Anderson et al. (1988), but it was equal to four for the scaled partition function[3]. Consequently, the modeled line intensities from the synthetic spectra were underestimated by a factor of four, and thus, the derived column density is overestimated by the same factor.

[3] See explanation at https://cdms.astro.uni-koeln.de/classic/predictions/description.html; update November 2023.

Another effect also comes into play through the derived excitation temperature: Jørgensen et al. (2018) derived a temperature of 321 ± 33 K from a rotation diagram fit (Fig. 1 in that paper) and categorized CH_3OD as being one of the species belonging to the "high-temperature" group (300 versus 125 K) of species. However, the new spectroscopic data appear to drive the best-fit excitation temperature toward lower values. The reason for this is illustrated with an example in Fig. 4 that shows a zoom-in on a specific frequency range between 362.5 and 362.9 GHz, which harbors several prominent CH_3OD transitions.

The upper part of the figure shows a comparison of the best-fit synthetic spectrum to the PILS data using the spectroscopy utilized in Jørgensen et al. (2018) and the spectroscopy of this paper for an excitation temperature of 300 K and a column density of $N = 4.5 \times 10^{16}$ cm^{-2} (the best-fit column density of CH_3OD derived in Jørgensen et al. 2018, corrected for the factor of four error mentioned above). As shown, the fits are very close

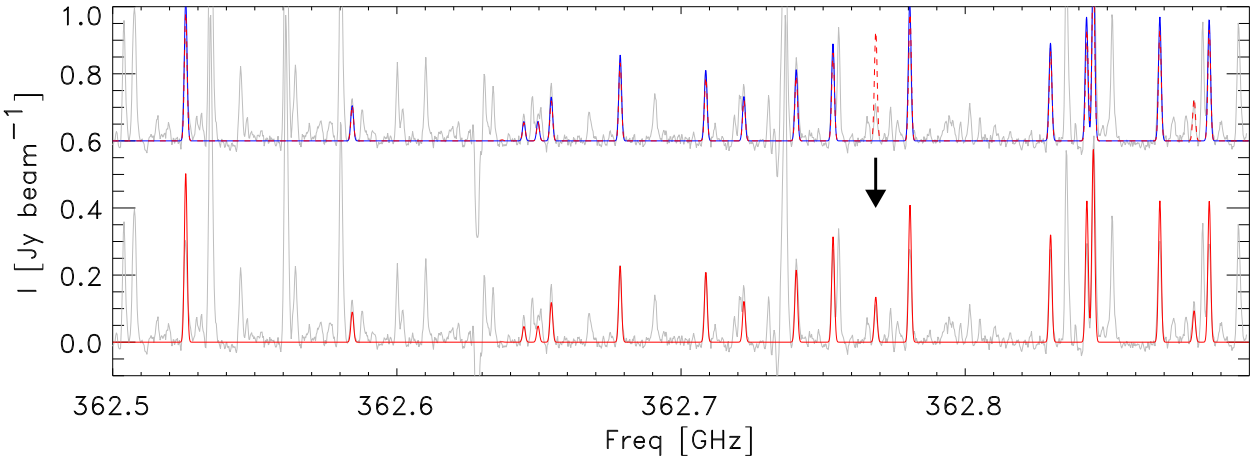

Fig. 4. Comparison between the observed PILS spectrum and the synthetic spectra obtained using the (old) spectroscopic data utilized in Jørgensen et al. (2018) (in blue) and the current spectroscopy (in red). The two synthetic spectra at an offset of 0.6 Jy beam^{-1} correspond to the prediction from the fit of the 2018 paper (solid blue curve) and current spectroscopy (dashed red curve), adopting the excitation temperature of 300 K from Jørgensen et al. (2018) and the column density from that same paper corrected for the factor of four error discussed in Sect. 5 ($N = 4.5 \times 10^{16}$ cm^{-2}). These two synthetic spectra are virtually identical except for two high excitation transitions at 362.7685 and 362.8805 GHz, where the new spectroscopic model demonstrates one clearly overpredicted transition (marked by an arrow). The synthetic spectrum at an offset of 0 Jy/beam correspond to the prediction with the lower inferred excitation temperature from the analysis summarized in Table 2, shown with a red curve. As can be seen, this spectrum matches well the high excitation 362.7685 and 362.8805 GHz transitions, which were not included in the old spectroscopy. These two lines come out at appropriate intensities in comparison to the observations within the uncertainties of the model.

except for one transition (v_t = 0, A-type, $22_{1-,22} - 22_{0+,22}$) at 362.7685 GHz, which has a high upper energy level that was not included in the old spectroscopy. This line with the high upper energy level of 563 K is significantly overproduced, with a high excitation temperature of 300 K, and consequently drives the fit toward a lower value. The spectral range also includes one v_t = 1 transition at 362.8805 GHz (E_{up} of 343 K) that is included in the new spectroscopy, but not in the original spectroscopy utilized in Jørgensen et al. (2018). The observed feature is well matched with the predictions from the 300 K fit of the 2018 analysis (even though it was not included there). With the lower excitation temperature fit (lower panel of Fig. 4), its line strength is slightly below (30%) the observed spectrum and the 300 K fit, but it is still in agreement within the uncertainties. The lower synthetic spectrum corresponds to the excitation temperature lowered to the value of Table 2 and the best-fit column density from the current analysis.

On the other hand, an important caveat here is of course that it is likely that there are gradients in temperatures, column densities, and extents of the emission along the line of sight. The fact that the higher excitation transitions from the new data are overproduced may also reflect that they represent more compact emission with smaller filling factors compared to the beam. If higher excitation transitions stem from a region that is significantly smaller than the beam size (0.5″), then our synthetic spectrum fitting would overestimate the source size. This effect could be compensated by driving the fit to lower excitation temperatures. However, fitting lower and higher excitation transitions separately is not a solution because the lower excitation transitions would be excited in high-temperature regions as well. Such gradients in temperature and differences in the extents of the high versus low excited transitions would of course also affect the line optical thickness (underestimating it for the lines tracing more compact emission). However, considering the lines according to their optical thickness, it is mainly the lower excited transitions that are likely to become optically thick, and those, in fact, do show extended emission relative to the beam (see Fig. 2 in Jørgensen et al. 2018 for the spatial distribution of various methanol isotopologs in lines with E_{up} on the order of 150−300 K). Without dedicated higher spatial resolution observations to use as constraints, it makes little sense to introduce more free parameters into the synthetic spectrum fitting. In any case, this discussion illustrates the importance of complete and updated spectroscopy, and it also emphasizes the need for using the comparisons between the observed spectra and synthetic models also including predictions for transitions that would not directly be predicted to be observed.

The newly determined best-fitting D/H ratio for CH_3OD is (0.32 ± 0.09)%. In contrast to what was previously thought, this implies that the D/H ratio in the hydroxy group of methanol does not match the D/H ratio in the methyl group of methanol. Including the statistical correction of three, the methyl group deuteration is (2.4 ± 0.72)% (Jørgensen et al. 2018), while the newly determined hydroxy group deuteration is a factor of ∼7.5 lower. This results in the hydroxy group of methanol having the lowest D/H ratio of all molecules with a measured D/H ratio in IRAS 16293-2422 B thus far. This is consistent with laboratory experiments that have demonstrated that deuteration in the hydroxy group is a lot less efficient than deuteration in the methyl group (Nagaoka et al. 2005, 2007; Hidaka et al. 2009); however, there are contrasts with the hydroxy group deuterated isotopologs of ethanol and formic acid with D/H ratios on the order of a few percent in IRAS 16293-2422 B (Jørgensen et al. 2018). This points to the fact that our understanding of the synthesis of complex organic molecules and their deuteration remains incomplete.

6. Conclusions

We have carried out an extensive study of the torsion-rotation spectrum of CH_3OD using a torsion-rotation RAM Hamiltonian. The new microwave measurements were performed in the broad frequency range from 34.4 GHz to 1.35 THz. Transitions involving the v_t = 0, 1, and 2 torsional states with J up to 51 and K_a up to 18 were assigned and analyzed in the current work. The second torsional state posed some problems in obtaining a fit

within experimental uncertainties using our current model, as was the case in our earlier investigations of CD_3OH and CD_3OD. We suspect perturbations by intervibrational interactions, which arise from low-lying small-amplitude vibrations of CH_3OD and transfer down to lower torsional states via torsion-rotation interactions, as the main reason for this. Therefore, we concentrated our efforts on refining the theoretical model for the ground and the first excited torsional states only, as in our studies of CD_3OH and CD_3OD. We achieved a fit well within the experimental uncertainties, with a weighted rms deviation of 0.85 for the dataset, which consists of 4758 far-infrared and 10163 microwave line frequencies.

We carried out calculations of the ground and first excited torsional states' spectra on the basis of our results and used these calculations to reinvestigate CH_3OD in data from PILS, which is a spectral survey of the deeply embedded low-mass protostar IRAS 16293−2422 performed with ALMA. Both, $v_t = 0$ and $v_t = 1$ transitions are observed in these data. The new accurately determined value for the column density of CH_3OD is a factor of ∼5.5 lower than earlier estimates. This implies a D/H ratio of $(0.32 \pm 0.09)\%$ in the hydroxy group of methanol, which is a factor of ∼7.5 lower than the D/H ratio in its methyl group. Further investigations are needed in order to understand the synthesis of deuterated complex organic molecules.

Acknowledgements. We acknowledge support by the Deutsche Forschungsgemeinschaft via the collaborative research center SFB 956 (project ID 184018867) project B3 and SFB 1601 (project ID 500700252) projects A4 and Inf as well as the Gerätezentrum SCHL 341/15-1 ("Cologne Center for Terahertz Spectroscopy"). The research in Kharkiv and Braunschweig was carried out under support of the Volkswagen foundation. The assistance of the Science and Technology Center in the Ukraine is acknowledged (STCU partner project P756). J.K.J. is supported by the Independent Research Fund Denmark (grant number 0135-00123B). R.M.L. received support from the Natural Sciences and Engineering Research Council of Canada. M.N.D. acknowledges the Holcim Foundation Stipend, the Swiss National Science Foundation (SNSF) Ambizione grant number 180079, the Center for Space and Habitability (CSH) Fellowship, and the IAU Gruber Foundation Fellowship. V.V.I. acknowledges financial support from Deutsche Forschungsgemeinschaft (grant number BA2176/9-1). E. Alekseev gratefully acknowledges financial support from Centre National de la Recherche Scientifique (CNRS, France) and from Université de Lille (France). Our research benefited from NASA's Astrophysics Data System (ADS). This paper makes use of the following ALMA data: ADS/JAO.ALMA # 2013.1.00278.S. ALMA is a partnership of ESO (representing its member states), NSF (USA) and NINS (Japan), together with NRC (Canada), MOST and ASIAA (Taiwan), and KASI (Republic of Korea), in cooperation with the Republic of Chile. The Joint ALMA Observatory is operated by ESO, AUI/NRAO and NAOJ.

References

Agúndez, M., Marcelino, N., Cernicharo, J., Roueff, E., & Tafalla, M. 2019, A&A, 625, A147
Alekseev, E. A., Ilyushin, V. V., Budnikov, V. V., Pogrebnyak, M. L., & Kniazkov, L. B. 2023, Radio Phys. Radio Astron., 28, 257
Ambrose, H. E., Shirley, Y. L., & Scibelli, S. 2021, MNRAS, 501, 347
Anderson, T., Crownover, R. L., Herbst, E., & De Lucia, F. C. 1988, ApJS, 67, 135
Anderson, T., Herbst, E., & De Lucia, F. C. 1993, J. Mol. Spectrosc., 159, 410
Ball, J. A., Gottlieb, C. A., Lilley, A. E., & Radford, H. E. 1970, ApJ, 162, L203
Belloche, A., Müller, H. S. P., Garrod, R. T., & Menten, K. M. 2016, A&A, 587, A91
Bermudez, C., Motiyenko, R., Cabezas, C., et al. 2022, Spectrochim. Acta A, 274, 121071
Bøgelund, E. G., McGuire, B. A., Ligterink, N. F. W., et al. 2018, A&A, 615, A88
Brünken, S., Sipilä, O., Chambers, E. T., et al. 2014, Nature, 516, 219
Ceccarelli, C., Caselli, P., Herbst, E., Tielens, A. G. G. M., & Caux, E. 2007, in Protostars and Planets V, eds. B. Reipurth, D. Jewitt, & K. Keil, 47
Chacón-Tanarro, A., Caselli, P., Bizzocchi, L., et al. 2019, A&A, 622, A141
Chantzos, J., Spezzano, S., Caselli, P., et al. 2018, ApJ, 863, 126
Crapsi, A., Caselli, P., Walmsley, C. M., et al. 2005, ApJ, 619, 379
Drozdovskaya, M. N., Coudert, L. H., Margulès, L., et al. 2022, A&A, 659, A69
Duan, Y. B., Ozier, I., Tsunekawa, S., & Takagi, K. 2003, J. Mol. Spectrosc., 218, 95
Endres, C. P., Schlemmer, S., Schilke, P., Stutzki, J., & Müller, H. S. P. 2016, J. Mol. Spectrosc., 327, 95
Fontani, F., Palau, A., Caselli, P., et al. 2011, A&A, 529, L7
Foreman-Mackey, D., Hogg, D. W., Lang, D., & Goodman, J. 2013, PASP, 125, 306
Harju, J., Sipilä, O., Brünken, S., et al. 2017, ApJ, 840, 63
Herbst, E., Messer, J. K., DeLucia, F. C., & Helminger, P. 1984, J. Mol. Spectrosc., 108, 42
Hidaka, H., Watanabe, M., Kouchi, A., & Watanabe, N. 2009, ApJ, 702, 291
Hougen, J. T., Kleiner, I., & Godefroid, M. 1994, J. Mol. Spectrosc., 163, 559
Ilyushin, V. 2004, J. Mol. Spectrosc., 227, 140
Ilyushin, V. V., Kisiel, Z., Pszczókowski, L., Mäder, H., & Hougen, J. T. 2010, J. Mol. Spectrosc., 259, 26
Ilyushin, V. V., Endres, C. P., Lewen, F., Schlemmer, S., & Drouin, B. J. 2013, J. Mol. Spectrosc., 290, 31
Ilyushin, V. V., Müller, H. S. P., Jørgensen, J. K., et al. 2022, A&A, 658, A127
Ilyushin, V. V., Müller, H. S. P., Jørgensen, J. K., et al. 2023, A&A, 677, A49
Jørgensen, J. K., van der Wiel, M. H. D., Coutens, A., et al. 2016, A&A, 595, A117
Jørgensen, J. K., Müller, H. S. P., Calcutt, H., et al. 2018, A&A, 620, A170
Kaushik, V. K., Takagi, K., & Matsumura, C. 1980, J. Mol. Spectrosc., 82, 418
Kirtman, B. 1962, J. Chem. Phys., 37, 2516
Lees, R. M., & Baker, J. G. 1968, J. Chem. Phys., 48, 5299
Lees, R. M., Xu, L.-H., & Billinghurst, B. E. 2013, Can. J. Phys., 91, 949
Lin, C. C., & Swalen, J. D. 1959, Rev. Mod. Phys., 31, 841
Lin, Y., Spezzano, S., & Caselli, P. 2023, A&A, 669, L6
Lovas, F. J. 1986, J. Phys. Chem. Ref. Data, 15, 251
Lundsgaard, A., Petersen, J. C., & Henningsen, J. 1994, J. Mol. Spectrosc., 167, 131
Manigand, S., Calcutt, H., Jørgensen, J. K., et al. 2019, A&A, 623, A69
Martin-Drumel, M. A., van Wijngaarden, J., Zingsheim, O., et al. 2015, J. Mol. Spectrosc., 307, 33
Mauersberger, R., Henkel, C., Jacq, T., & Walmsley, C. M. 1988, A&A, 194, L1
Mekhtiev, M. A., Godfrey, P. D., & Hougen, J. T. 1999, J. Mol. Spectrosc., 194, 171
Motiyenko, R. A., Ilyushin, V. V., Demaison, J., et al. 2020, J. Mol. Struct., 1213, 128037
Mukhopadhyay, I. 1999, Spectrochim. Acta A, 55, 1767
Mukhopadhyay, I. 2021, Infrared Phys. Technol., 116, 103605
Mukhopadhyay, I., & Duan, Y.-B. 2000, Chem. Phys., 257, 91
Mukhopadhyay, I., Gupta, P. K., Moruzzi, G., Winnewisser, B. P., & Winnewisser, M. 1997, J. Mol. Spectrosc., 186, 15
Mukhopadhyay, I., Duan, Y. B., & Takagi, K. 1998, Spectrochim. Acta A, 54, 1325
Müller, H. S. P., Thorwirth, S., Roth, D. A., & Winnewisser, G. 2001, A&A, 370, L49
Müller, H. S. P., Schlöder, F., Stutzki, J., & Winnewisser, G. 2005, J. Mol. Struct., 742, 215
Müller, H. S. P., Zingsheim, O., Wehres, N., et al. 2017, J. Phys. Chem. A, 121, 7121
Müller, H. S. P., Belloche, A., Lewen, F., et al. 2021, J. Mol. Spectrosc., 378, 111449
Müller, H. S. P., Guillemin, J.-C., Lewen, F., & Schlemmer, S. 2022, J. Mol. Spectrosc., 384, 111584
Müller, H. S. P., Jørgensen, J. K., Guillemin, J.-C., Lewen, F., & Schlemmer, S. 2023, MNRAS, 518, 185
Nagaoka, A., Watanabe, N., & Kouchi, A. 2005, ApJ, 624, L29
Nagaoka, A., Watanabe, N., & Kouchi, A. 2007, J. Phys. Chem. A, 111, 3016
Nakagawa, K., Tsunekawa, S., & Kojima, T. 1987, J. Mol. Spectrosc., 126, 329
Neill, J. L., Crockett, N. R., Bergin, E. A., Pearson, J. C., & Xu, L.-H. 2013, ApJ, 777, 85
Nishikawa, T. 1956, J. Phys. Soc. Jpn, 11, 781
Okoda, Y., Oya, Y., Imai, M., et al. 2022, ApJ, 935, 136
Ratajczak, A., Taquet, V., Kahane, C., et al. 2011, A&A, 528, L13
Smirnov, I. A., Alekseev, E. A., Ilyushin, V. V., et al. 2014, J. Mol. Spectrosc., 295, 44
Takagi, K., & Kaushik, V. K. 1982, J. Mol. Spectrosc., 93, 438
Taquet, V., Bianchi, E., Codella, C., et al. 2019, A&A, 632, A19
van Gelder, M. L., Jaspers, J., Nazari, P., et al. 2022, A&A, 667, A136
Venkateswarlu, P., Edwards, H. D., & Gordy, W. 1955, J. Chem. Phys., 23, 1195
Walsh, M. S., Xu, L.-H., Lees, R. M., et al. 2000, J. Mol. Spectrosc., 204, 60
Wilkins, O. H., & Blake, G. A. 2022, J. Phys. Chem. A, 126, 6473
Xu, L.-H., Fisher, J., Lees, R. M., et al. 2008, J. Mol. Spectrosc., 251, 305
Xu, L.-H., Lees, R. M., Crabbe, G. T., et al. 2012, J. Chem. Phys., 137, 104313
Zakharenko, O., Ilyushin, V. V., Lewen, F., et al. 2019, A&A, 629, A73

Appendix A: Parameters of the RAM Hamiltonian for the CH_3OD molecule

Table A.1. Fitted parameters of the RAM Hamiltonian for the CH_3OD molecule.

n_{tr}[a]	Par.[b]	Operator[c]	Value[d,e]
$2_{2,0}$	$(1/2)V_3$	$(1-\cos 3\alpha)$	183.171569(21)
$2_{2,0}$	F	p_α^2	17.42797209(17)
$2_{1,1}$	ρ	$P_a p_\alpha$	0.6993446726(21)
$2_{0,2}$	A_{RAM}	P_a^2	3.675099(14)
$2_{0,2}$	B_{RAM}	P_b^2	0.783150(12)
$2_{0,2}$	C_{RAM}	P_c^2	0.733527(12)
$2_{0,2}$	$2D_{ab}$	$(1/2)\{P_a,P_b\}$	0.055955652(61)
$4_{4,0}$	$(1/2)V_6$	$(1-\cos 6\alpha)$	−0.807349(95)
$4_{4,0}$	F_m	p_α^4	$-0.2945328(17)\times10^{-2}$
$4_{3,1}$	ρ_m	$P_a p_\alpha^3$	$-0.11189627(44)\times10^{-1}$
$4_{2,2}$	V_{3J}	$P^2(1-\cos 3\alpha)$	$-0.2211486(94)\times10^{-2}$
$4_{2,2}$	V_{3K}	$P_a^2(1-\cos 3\alpha)$	$0.125539(11)\times10^{-1}$
$4_{2,2}$	V_{3bc}	$(P_b^2-P_c^2)(1-\cos 3\alpha)$	$-0.137249(22)\times10^{-3}$
$4_{2,2}$	V_{3ab}	$(1/2)\{P_a,P_b\}(1-\cos 3\alpha)$	$0.15619469(62)\times10^{-1}$
$4_{2,2}$	F_J	$P^2 p_\alpha^2$	$-0.8417192(26)\times10^{-4}$
$4_{2,2}$	F_K	$P_a^2 p_\alpha^2$	$-0.16465226(55)\times10^{-1}$
$4_{2,2}$	F_{bc}	$(P_b^2-P_c^2)p_\alpha^2$	$-0.8781804(46)\times10^{-4}$
$4_{2,2}$	F_{ab}	$(1/2)\{P_a,P_b\}p_\alpha^2$	$0.123059(61)\times10^{-3}$
$4_{2,2}$	D_{3ac}	$(1/2)\{P_a,P_c\}\sin 3\alpha$	$0.287840(14)\times10^{-1}$
$4_{1,3}$	ρ_J	$P^2 P_a p_\alpha$	$-0.12144162(39)\times10^{-3}$
$4_{1,3}$	ρ_K	$P_a^3 p_\alpha$	$-0.10794357(36)\times10^{-1}$
$4_{1,3}$	ρ_{bc}	$(1/2)\{P_a,(P_b^2-P_c^2)\}p_\alpha$	$-0.1589380(32)\times10^{-3}$
$4_{1,3}$	ρ_{ab}	$(1/2)\{P_a^2,P_b\}p_\alpha$	$0.115410(57)\times10^{-3}$
$4_{0,4}$	$-\Delta_J$	P^4	$-0.144728(12)\times10^{-5}$
$4_{0,4}$	$-\Delta_{JK}$	$P^2 P_a^2$	$-0.46863(83)\times10^{-4}$
$4_{0,4}$	$-\Delta_K$	P_a^4	$-0.26562002(84)\times10^{-2}$
$4_{0,4}$	$-2\delta_J$	$P^2(P_b^2-P_c^2)$	$-0.1984984(31)\times10^{-6}$
$4_{0,4}$	$-2\delta_K$	$(1/2)\{P_a^2,(P_b^2-P_c^2)\}$	$-0.726533(26)\times10^{-4}$
$4_{0,4}$	D_{abJ}	$(1/2)P^2\{P_a,P_b\}$	$-0.69723(14)\times10^{-6}$
$6_{6,0}$	$(1/2)V_9$	$(1-\cos 9\alpha)$	$0.1588(23)\times10^{-1}$
$6_{6,0}$	F_{mm}	p_α^6	$0.22823(16)\times10^{-5}$
$6_{5,1}$	ρ_{mm}	$P_a p_\alpha^5$	$0.150802(69)\times10^{-4}$
$6_{4,2}$	V_{6J}	$P^2(1-\cos 6\alpha)$	$-0.6128(78)\times10^{-4}$
$6_{4,2}$	V_{6K}	$P_a^2(1-\cos 6\alpha)$	$0.1056(50)\times10^{-3}$
$6_{4,2}$	V_{6bc}	$(P_b^2-P_c^2)(1-\cos 6\alpha)$	$-0.28947(72)\times10^{-4}$
$6_{4,2}$	V_{6ab}	$(1/2)\{P_a,P_b\}(1-\cos 6\alpha)$	$-0.2335(10)\times10^{-4}$
$6_{4,2}$	F_{mJ}	$P^2 p_\alpha^4$	$0.25716(24)\times10^{-7}$
$6_{4,2}$	F_{mK}	$P_a^2 p_\alpha^4$	$0.40075(13)\times10^{-4}$
$6_{4,2}$	D_{6ac}	$(1/2)\{P_a,P_c\}\sin 6\alpha$	$0.10499(12)\times10^{-3}$
$6_{3,3}$	ρ_{mJ}	$P^2 P_a p_\alpha^3$	$0.89234(68)\times10^{-7}$
$6_{3,3}$	ρ_{mK}	$P_a^3 p_\alpha^3$	$0.55525(14)\times10^{-4}$
$6_{3,3}$	ρ_{3bc}	$(1/2)\{P_a,P_b,P_c,p_\alpha,\sin 3\alpha\}$	$0.17326(13)\times10^{-5}$
$6_{2,4}$	V_{3JJ}	$P^4(1-\cos 3\alpha)$	$0.13288(18)\times10^{-7}$
$6_{2,4}$	V_{3JK}	$P^2 P_a^2(1-\cos 3\alpha)$	$-0.108198(83)\times10^{-5}$
$6_{2,4}$	V_{3KK}	$P_a^4(1-\cos 3\alpha)$	$0.12335(14)\times10^{-5}$
$6_{2,4}$	V_{3bcJ}	$P^2(P_b^2-P_c^2)(1-\cos 3\alpha)$	$0.54564(17)\times10^{-8}$
$6_{2,4}$	V_{3bcK}	$(1/2)\{P_a^2,(P_b^2-P_c^2)\}(1-\cos 3\alpha)$	$-0.6019(59)\times10^{-7}$
$6_{2,4}$	V_{3b2c2}	$(1/2)\{P_b^2,P_c^2\}\cos 3\alpha$	$0.36950(15)\times10^{-7}$
$6_{2,4}$	V_{3abJ}	$(1/2)P^2\{P_a,P_b\}(1-\cos 3\alpha)$	$-0.34986(11)\times10^{-6}$
$6_{2,4}$	V_{3abK}	$(1/2)\{P_a^3,P_b\}(1-\cos 3\alpha)$	$-0.16693(13)\times10^{-5}$
$6_{2,4}$	V_{3abc2}	$(1/2)\{P_a,P_b,P_c^2\}\cos 3\alpha$	$-0.41168(30)\times10^{-6}$
$6_{2,4}$	F_{JJ}	$P^4 p_\alpha^2$	$0.52398(53)\times10^{-9}$
$6_{2,4}$	F_{JK}	$P^2 P_a^2 p_\alpha^2$	$0.120708(76)\times10^{-6}$
$6_{2,4}$	F_{KK}	$P_a^4 p_\alpha^2$	$0.426507(90)\times10^{-4}$
$6_{2,4}$	F_{bcJ}	$P^2(P_b^2-P_c^2)p_\alpha^2$	$0.747(35)\times10^{-9}$

Table A.1. continued..

n_{tr}[a]	Par.[b]	Operator[c]	Value[d,e]
$6_{2,4}$	F_{abJ}	$(1/2)P^2\{P_a,P_b\}p_\alpha^2$	$-0.1940(17)\times10^{-8}$
$6_{2,4}$	D_{3acJ}	$(1/2)P^2\{P_a,P_c\}\sin3\alpha$	$-0.21496(33)\times10^{-6}$
$6_{2,4}$	D_{3acK}	$(1/2)\{P_a^3,P_c\}\sin3\alpha$	$-0.27643(22)\times10^{-5}$
$6_{2,4}$	D_{3bcJ}	$(1/2)P^2\{P_b,P_c\}\sin3\alpha$	$-0.1440(78)\times10^{-7}$
$6_{2,4}$	D_{3acb2}	$(1/2)\{P_a,P_b^2,P_c\}\sin3\alpha$	$-0.63621(23)\times10^{-6}$
$6_{2,4}$	D_{3bcbc}	$(1/2)(\{P_b^3,P_c\}-\{P_b,P_c^3\})\sin3\alpha$	$-0.15526(13)\times10^{-7}$
$6_{1,5}$	ρ_{JJ}	$P^4P_ap_\alpha$	$0.76489(73)\times10^{-9}$
$6_{1,5}$	ρ_{JK}	$P^2P_a^3p_\alpha$	$0.72735(40)\times10^{-7}$
$6_{1,5}$	ρ_{KK}	$P_a^5p_\alpha$	$0.173086(31)\times10^{-4}$
$6_{1,5}$	ρ_{bcJ}	$(1/2)P^2\{P_a,(P_b^2-P_c^2)\}p_\alpha$	$0.1779(33)\times10^{-8}$
$6_{0,6}$	Φ_J	P^6	$-0.839(30)\times10^{-13}$
$6_{0,6}$	Φ_{JK}	$P^4P_a^2$	$0.30696(29)\times10^{-9}$
$6_{0,6}$	Φ_{KJ}	$P^2P_a^4$	$0.17819(12)\times10^{-7}$
$6_{0,6}$	Φ_K	P_a^6	$0.290869(45)\times10^{-5}$
$6_{0,6}$	$2\phi_J$	$P^4(P_b^2-P_c^2)$	$0.6901(12)\times10^{-12}$
$6_{0,6}$	$2\phi_{JK}$	$(1/2)P^2\{P_a^2,(P_b^2-P_c^2)\}$	$0.102073(94)\times10^{-8}$
$6_{0,6}$	$2\phi_K$	$(1/2)\{P_a^4,(P_b^2-P_c^2)\}$	$0.2973(18)\times10^{-8}$
$6_{0,6}$	D_{b2c2bc}	$(1/2)(\{P_b^4,P_c^2\}-\{P_b^2,P_c^4\})$	$-0.32957(53)\times10^{-11}$
$6_{0,6}$	D_{abJK}	$(1/2)P^2\{P_a^3,P_b\}$	$0.1662(15)\times10^{-8}$
$6_{0,6}$	D_{abc4}	$(1/2)\{P_a,P_b,P_c^4\}$	$0.1892(15)\times10^{-10}$
$8_{8,0}$	F_{mmm}	p_α^8	$0.2592(24)\times10^{-8}$
$8_{6,2}$	V_{9J}	$P^2(1-\cos9\alpha)$	$0.3021(47)\times10^{-3}$
$8_{6,2}$	V_{9K}	$P_a^2(1-\cos9\alpha)$	$-0.657(12)\times10^{-3}$
$8_{6,2}$	F_{mmK}	$P_a^2p_\alpha^6$	$-0.5042(33)\times10^{-7}$
$8_{6,2}$	D_{9bc}	$(1/2)\{P_b,P_c\}\sin9\alpha$	$0.78071(91)\times10^{-4}$
$8_{5,3}$	ρ_{mmK}	$P_a^3p_\alpha^5$	$-0.16973(94)\times10^{-6}$
$8_{5,3}$	ρ_{3bcm}	$(1/2)\{P_a,P_b,P_c,p_\alpha^3,\sin3\alpha\}$	$-0.770(13)\times10^{-8}$
$8_{4,4}$	V_{6JJ}	$P^4(1-\cos6\alpha)$	$0.2170(71)\times10^{-8}$
$8_{4,4}$	V_{6JK}	$P^2P_a^2(1-\cos6\alpha)$	$-0.5615(58)\times10^{-6}$
$8_{4,4}$	V_{6KK}	$P_a^4(1-\cos6\alpha)$	$0.1808(27)\times10^{-6}$
$8_{4,4}$	V_{6bcJ}	$P^2(P_b^2-P_c^2)(1-\cos6\alpha)$	$0.14457(44)\times10^{-8}$
$8_{4,4}$	V_{6bcK}	$(1/2)\{P_a^2,(P_b^2-P_c^2)\}(1-\cos6\alpha)$	$0.4650(41)\times10^{-7}$
$8_{4,4}$	F_{mKK}	$P_a^4p_\alpha^4$	$-0.2700(13)\times10^{-6}$
$8_{4,4}$	D_{6bcJ}	$(1/2)P^2\{P_b,P_c\}\sin6\alpha$	$-0.461(16)\times10^{-9}$
$8_{4,4}$	D_{6bcbc}	$(1/2)(\{P_b,P_c^3\}-\{P_b^3,P_c\})\sin6\alpha$	$0.2259(44)\times10^{-8}$
$8_{4,4}$	D_{3acb2m}	$(1/2)\{P_a,P_b^2,P_c,p_\alpha^2,\sin3\alpha\}$	$0.859(12)\times10^{-9}$
$8_{3,5}$	ρ_{mKK}	$P_a^5p_\alpha^3$	$-0.2464(11)\times10^{-6}$
$8_{3,5}$	ρ_{3bcK}	$(1/2)\{P_a^3,P_b,P_c,p_\alpha,\sin3\alpha\}$	$0.4437(26)\times10^{-7}$
$8_{2,6}$	V_{3JJJ}	$P^6(1-\cos3\alpha)$	$-0.576(19)\times10^{-13}$
$8_{2,6}$	V_{3KKK}	$P_a^6(1-\cos3\alpha)$	$-0.3463(78)\times10^{-9}$
$8_{2,6}$	V_{3bcKK}	$(1/2)\{P_a^4,(P_b^2-P_c^2)\}(1-\cos3\alpha)$	$-0.2770(18)\times10^{-8}$
$8_{2,6}$	$V_{3b2c2bc}$	$(1/2)(\{P_b^4,P_c^2\}-\{P_b^2,P_c^4\})\cos3\alpha$	$0.7702(54)\times10^{-12}$
$8_{2,6}$	V_{3abJJ}	$(1/2)P^4\{P_a,P_b\}(1-\cos3\alpha)$	$0.3300(70)\times10^{-11}$
$8_{2,6}$	V_{3abc4}	$(1/2)\{P_a,P_b,P_c^4\}\cos3\alpha$	$0.1252(17)\times10^{-10}$
$8_{2,6}$	F_{JJJ}	$P^6p_\alpha^2$	$-0.363(21)\times10^{-14}$
$8_{2,6}$	F_{KKK}	$P_a^6p_\alpha^2$	$-0.13293(51)\times10^{-6}$
$8_{2,6}$	D_{3acJJ}	$(1/2)P^4\{P_a,P_c\}\sin3\alpha$	$-0.2388(78)\times10^{-11}$
$8_{2,6}$	D_{3acKK}	$(1/2)\{P_a^5,P_c\}\sin3\alpha$	$0.3398(79)\times10^{-9}$
$8_{2,6}$	D_{3bcJJ}	$(1/2)P^4\{P_b,P_c\}\sin3\alpha$	$0.4091(84)\times10^{-12}$
$8_{2,6}$	D_{3bcKK}	$(1/2)\{P_a^4,P_b,P_c\}\sin3\alpha$	$0.2557(16)\times10^{-7}$
$8_{2,6}$	D_{3acb2J}	$(1/2)P^2\{P_a,P_b^2,P_c\}\sin3\alpha$	$0.1579(16)\times10^{-10}$
$8_{2,6}$	D_{3acb2K}	$(1/2)\{P_a^3,P_b^2,P_c\}\sin3\alpha$	$-0.5322(48)\times10^{-9}$
$8_{2,6}$	D_{3bcbcJ}	$(1/2)P^2(\{P_b^3,P_c\}-\{P_b,P_c^3\})\sin3\alpha$	$0.3740(28)\times10^{-12}$
$8_{1,7}$	ρ_{JJJ}	$P^6P_ap_\alpha$	$-0.710(29)\times10^{-14}$
$8_{1,7}$	ρ_{KKK}	$P_a^7p_\alpha$	$-0.3969(14)\times10^{-7}$
$8_{0,8}$	L_J	P^8	$-0.1082(61)\times10^{-16}$
$8_{0,8}$	L_{JJK}	$P^6P_a^2$	$-0.355(10)\times10^{-14}$

Table A.1. continued..

n_{tr}[a]	Par.[b]	Operator[c]	Value[d,e]
$8_{0,8}$	L_K	P_a^8	$-0.5083(16) \times 10^{-8}$
$8_{0,8}$	$2l_K$	$(1/2)\{P_a^6,(P_b^2 - P_c^2)\}$	$-0.254(13) \times 10^{-12}$
$10_{8,2}$	V_{12J}	$P^2(1 - \cos 12\alpha)$	$-0.992(16) \times 10^{-3}$
$10_{8,2}$	V_{12bc}	$(P_b^2 - P_c^2)(1 - \cos 12\alpha)$	$-0.8712(96) \times 10^{-4}$
$10_{6,4}$	V_{9JJ}	$P^4(1 - \cos 9\alpha)$	$-0.326(18) \times 10^{-8}$
$10_{6,4}$	V_{9JK}	$P^2P_a^2(1 - \cos 9\alpha)$	$0.2026(32) \times 10^{-5}$
$10_{6,4}$	V_{9b2c2}	$(1/2)\{P_b^2,P_c^2\} \cos 9\alpha$	$0.544(16) \times 10^{-8}$
$10_{6,4}$	D_{9acK}	$(1/2)\{P_a^3,P_c\} \sin 9\alpha$	$-0.5240(98) \times 10^{-6}$
$10_{6,4}$	D_{6acmK}	$(1/2)\{P_a^3,P_c,p_\alpha^2, \sin 6\alpha\}$	$0.1717(33) \times 10^{-7}$
$10_{4,6}$	V_{6JJJ}	$P^6(1 - \cos 6\alpha)$	$-0.551(35) \times 10^{-13}$
$10_{4,6}$	V_{6JKK}	$P^2P_a^4(1 - \cos 6\alpha)$	$0.8775(30) \times 10^{-9}$
$10_{4,6}$	V_{6KKK}	$P_a^6(1 - \cos 6\alpha)$	$0.214(14) \times 10^{-9}$
$10_{4,6}$	V_{6bcJJ}	$P^4(P_b^2 - P_c^2)(1 - \cos 6\alpha)$	$-0.808(19) \times 10^{-13}$
$10_{4,6}$	V_{6b2c2K}	$(1/2)\{P_a^2,P_b^2,P_c^2\} \cos 6\alpha$	$-0.580(19) \times 10^{-10}$
$10_{4,6}$	D_{6acKK}	$(1/2)\{P_a^5,P_c\} \sin 6\alpha$	$-0.842(15) \times 10^{-8}$
$10_{3,7}$	ρ_{3bcKK}	$(1/2)\{P_a^5,P_b,P_c,p_\alpha, \sin 3\alpha\}$	$0.1553(41) \times 10^{-11}$
$10_{2,8}$	V_{3JKKK}	$P^2P_a^6(1 - \cos 3\alpha)$	$0.548(14) \times 10^{-13}$
$10_{2,8}$	D_{3b3c3J}	$(1/2)P^2\{P_b^3,P_c^3\} \sin 3\alpha$	$-0.977(46) \times 10^{-16}$
$12_{8,4}$	V_{12JK}	$P^2P_a^2(1 - \cos 12\alpha)$	$-0.408(11) \times 10^{-5}$
$12_{6,6}$	V_{9JKK}	$P^2P_a^4(1 - \cos 9\alpha)$	$-0.23634(86) \times 10^{-8}$
$12_{6,6}$	V_{9b2c2K}	$(1/2)\{P_a^2,P_b^2,P_c^2\} \cos 9\alpha$	$0.639(42) \times 10^{-10}$
$12_{4,8}$	D_{6bcJJK}	$(1/2)P^4\{P_a^2,P_b,P_c\} \sin 6\alpha$	$0.492(18) \times 10^{-14}$

Notes. [a] n=t+r, where n is the total order of the operator, t is the order of the torsional part, and r is the order of the rotational part, respectively. The ordering scheme of Nakagawa et al. (1987) is used. [b] The parameter nomenclature is based on the subscript procedure of Xu et al. (2008). [c] $\{A, B, C, D, E\} = ABCDE + EDCBA$. $\{A, B, C, D\} = ABCD + DCBA$. $\{A, B, C\} = ABC + CBA$. $\{A, B\} = AB + BA$. The product of the operator in the third column of a given row and the parameter in the second column of that row gives the term actually used in the torsion-rotation Hamiltonian of the program, except for F, ρ, and $A_{\rm RAM}$, which occur in the Hamiltonian in the form $F(p_\alpha + \rho P_a)^2 + A_{\rm RAM}P_a^2$. [d] Values of the parameters are in units of reciprocal centimeters, except for ρ, which is unitless. [e] Statistical uncertainties are given in parentheses as one standard uncertainty in units of the last digits.

Appendix B: Corner plot of the second MCMC run of the CH_3OD computation for IRAS 16293-2422 B.

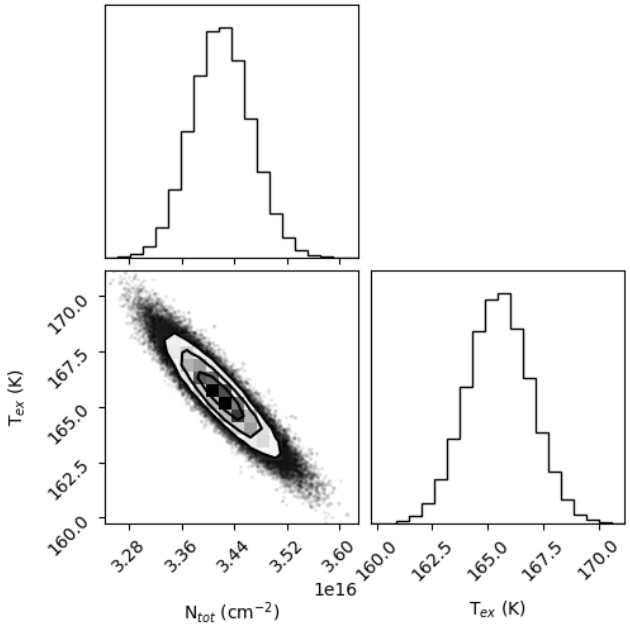

Fig. B.1. Corner plot of the second MCMC run of the CH_3OD computation for IRAS 16293-2422 B.